Experimental scheme for determining the Berry phase in two-dimensional quantum materials with a flat band

Li-Li Ye,[1] Cheng-Zhen Wang,[2] and Ying-Cheng Lai[1,3,*]

[1]*School of Electrical, Computer and Energy Engineering, Arizona State University, Tempe, Arizona 85287, USA*

[2]*Wave Transport in Complex Systems Lab, Department of Physics, Wesleyan University, Middletown, Connecticut 06459, USA*

[3]*Department of Physics, Arizona State University, Tempe, Arizona 85287, USA*

(Received 22 February 2024; revised 24 June 2024; accepted 22 July 2024; published 5 August 2024)

Experimentally feasible methods to determine the Berry phase, a fundamental quantity characterizing a quantum material, are often needed in applications. We develop an approach to detecting the Berry phase by using a class of two-dimensional (2D) Dirac materials with a flat band, the α-$\mathcal{T}_3$ lattices. The properties of this class of quantum materials are controlled by a single parameter $0 \leqslant \alpha \leqslant 1$, where the left and right end points correspond to graphene with pseudospin-$\frac{1}{2}$ and the dice lattice with pseudospin-1 Dirac-Weyl quasiparticles, respectively, and each specific value of α represents a material with a unique Berry phase. Applying a constant electric field to the α-$\mathcal{T}_3$ lattice, we calculate the resulting electric current and find a one-to-one correspondence between the current and the Berry phase in both the linear and nonlinear response regimes. In the linear (Kubo) regime, the main physics is the *Zitterbewegung* effect. In the nonlinear regime, the Schwinger mechanism dominates. Beyond the nonlinear regime, Bloch-Zener oscillations can arise. Measuring the current thus provides an effective and experimentally feasible way to determine the Berry phase for this spectrum of 2D quantum materials.

DOI: 10.1103/PhysRevB.110.075108

I. INTRODUCTION

The Berry phase (the geometric phase or the Pancharatnam-Berry phase) [1–3] of the electronic wave function is a fundamental characteristic of quantum materials and can have significant effects on material properties and physical phenomena such as polarization, magnetism, and quantum anomalous spin Hall effects [4]. The Berry phase arises when a parameter of the system completes a cycle of adiabatic changes: even as the parameter returns to its initial value, the wave function gains an extra phase of purely geometric origin. The value of the Berry phase depends on the nature of the quasiparticles which, in turn, depends on the specific quantum material. Given a family of quantum materials, the Berry phase is effectively a unique identifier of each material in the family. For example, monolayer graphene hosting a pair of Dirac cones and pseudospin-$\frac{1}{2}$ quasiparticles, the Berry phase is $\pm\pi$ associated, respectively, with the electronic states in the two Dirac cones [5,6]. For bilayer graphene, the Berry phase is 2π, which leads to unconventional quantum Hall effect [7]. For pseudospin-1 Dirac-Weyl materials, the Berry phase is zero [8,9]. In recent years, various two-dimensional (2D) Dirac materials have been discovered at a rapid pace [10–12], each carrying a unique type of quasiparticles with a unique value of the Berry phase. Given a new quantum material, knowing the Berry phase is thus of theoretical, experimental, and applied interests.

In principle, the phenomenon of Aharonov-Bohm interference provides an approach to assessing the Berry phase [13–15]. Take graphene as an example. For a circular graphene *p-n* junction resonator, due to the $\pm\pi$ Berry phase of the quasiparticles, as the strength of an external magnetic field is tuned, a sudden change in the energy of the angular-momentum states can occur, providing an indirect way to ascertain the value of the Berry phase [14,15]. For photonic crystals, their analogy with graphene was exploited to measure the geometric Berry phase by removing the dynamical phase [16]. For a general family of 2D Dirac-Weyl materials (the α-$\mathcal{T}_3$ lattices), the semiclassical dynamics of a chaotic cavity made of such a material were explored to infer its Berry phase [9]. In particular, by applying a gate voltage to generate a quasiconfinement of a certain geometric shape that generates chaos in the classical limit, a one-to-one correspondence between the exponential rate of particles escaping from the cavity and the Berry phase was identified. Despite the theoretical appeal of this semiclassical phenomenon, experimentally monitoring the decay of an ensemble of quasiparticles from a cavity of certain quantum material is not feasible at present.

In this paper, we present theoretical calculations leading to an experimentally feasible approach to detecting the Berry phase for the α-$\mathcal{T}_3$ lattice family whose material properties are controlled by a single parameter: $0 \leqslant \alpha \leqslant 1$. An α-$\mathcal{T}_3$ lattice has the honeycomb lattice as its base with an additional atom at the center of each hexagonal unit cell. In the tight-binding approximation, the center atom couples with any of the hexagonal atoms with the energy αt_ϵ, where t_ϵ is the nearest-neighbor coupling energy of the honeycomb lattice. Because of the center atom, an α-$\mathcal{T}_3$ lattice with $\alpha > 0$ possesses three distinct energy bands: a pair of Dirac cones

*Contact author: Ying-Cheng.Lai@asu.edu

and a flat band through the contact point of the two Dirac cones. As α increases from zero, a continuous spectrum of 2D Dirac-Weyl materials is generated: from the graphene ($\alpha = 0$) to the dice lattice ($\alpha = 1$), and the corresponding Berry phase can change from π to zero. As a result of the continuous decrease in the Berry phase, a number of pertinent physical phenomena change their characteristics. For example, the flat band plays an important role in the accurate quantization of the Hall conductivity in α-$\mathcal{T}_3$ lattices [17]. Wave-packet dynamics and *Zitterbewegung* [18], the effect of periodic kicks [19], Floquet dynamics driven by an electromagnetic field [20], the size effects on atomic collapse [21], and topological phase transitions [22] have also been explored in an α-$\mathcal{T}_3$ lattice. The orbital magnetic response [23] at the Dirac point changes from diamagnetic ($\alpha = 0$) to paramagnetic ($\alpha = 1$) and the nature of the Hall quantization [8] switches from relativistic to nonrelativistic. Moreover, the patterns of optical response [24] and magneto-optical modulation [25] change because they depend on the interband transitions among the three bands. Further, optical conductivity quantization and higher-order harmonic generation were observed [26], so was the effect of a broken flat band on the integer quantum Hall effect by the disorder or staggered lattice potential [27]. Experimentally, the α-$\mathcal{T}_3$ lattice has been realized in the critical doping material [28] $Hg_{1-x}Cd_xTe$. For $\alpha = 1$, the dice lattice described by the pseudospin-1 Dirac-Weyl Hamiltonian can be grown in the transition-metal oxide [29] $SrTiO_3/SrIrO_3/SrTiO_3$ or in graphene-In_2Te_2 bilayer [30].

We focus on the electric current density (or simply the current) produced when a constant electric field is applied to the α-$\mathcal{T}_3$ lattice. In the classical Drude picture, when driven by a constant electric field $\mathcal{E}$, the electron momentum in the ballistic transport regime increases with time: $q = e\mathcal{E}t$. Nevertheless, Dirac electrons will be excited "instantaneously" to the Fermi velocity (pinned to the "light cone") [31], where the excitation mechanism is described by the Schwinger effect [32] or the Landau-Zener dynamics [33,34] that occur where there are two avoided-crossing energy levels under the adiabatic evolution induced by the electric field. Another relevant phenomenon is Bloch oscillations [35,36] in the time evolution of the electronic states in a single energy band. When multiple bands without crossings are present, Bloch-Zener oscillations [37–39] can take place. For the α-$\mathcal{T}_3$ lattice, irregular Bloch-Zener oscillations [40] can arise, due to the mixed interference of the quantum states in multibands based on Landau-Zener-Stuckelberg-Majorana transitions [41,42]. In addition, the mass term associated with the Dirac electrons or a weak disorder can render a nonzero minimal conductivity that depends on the value of α [43]. Other relevant transport phenomena in the α-$\mathcal{T}_3$ lattice includes the linear response in graphene with the chiral anomaly and nonlinear response when the perturbation theory breaks down [44], as well as nonlinear conductivity with THz-induced charge transport [45]. Nonequilibrium dynamics beyond the linear response in three-dimensional (3D) Weyl semimetals [46] and nodal loop semimetals [47] have also been studied.

The main physical considerations behind our calculations of the current are as follows. On different timescales, the transport properties and the physical mechanisms are distinct. In particular, in the Kubo regime [31] under the weak field approximation, the average current density is saturated and dominated by the *Zitterbewegung* effect [48] originated from the interference between the energy bands, which defines the regime of linear response. A strong electric field places the system in the Schwinger regime [32], where the electrons are excited by the Schwinger mechanism in which the vacuum field loses energy to produce electron-positron pairs. The transition probabilities among the energy bands are described by the Landau-Zener dynamics [49], where the quasiparticles adiabatically evolve and transitions occur about the point at which the two levels are closest to each other but without crossing. In this regime, the current is proportional to the number of the excited particles, representing a nonlinear response. When the product of the electric field and time is comparable to the lattice constant, Bloch oscillations [35,36] become important in the Landau-Zener dynamics, leading to Bloch-Zener oscillations [37–39]. The main finding is a monotonic dependence of the current on the materials parameter α in both the linear and nonlinear response regimes, implying a one-to-one correspondence between the current and the Berry phase, thereby providing a possible experimental scheme to determine the latter.

II. CURRENT AND BERRY PHASE CALCULATION FOR α-$\mathcal{T}_3$ LATTICE

A. Zero-field effective Hamiltonian

To calculate the current and the Berry phases in an α-$\mathcal{T}_3$ lattice, we begin with the zero-field lattice Hamiltonian. The basic lattice structure is shown in Fig. 1(a), where there are three distinct atoms in a unit cell: A and B atoms belonging to the base hexagonal lattice, and C atom at the center of the unit cell. The tight-binding Hamiltonian is given by [23]

$$H = \begin{bmatrix} 0 & f_{\mathbf{p}}\cos\varphi & 0 \\ f_{\mathbf{p}}^*\cos\varphi & 0 & f_{\mathbf{p}}\sin\varphi \\ 0 & f_{\mathbf{p}}^*\sin\varphi & 0 \end{bmatrix}, \tag{1}$$

with

$$f_{\mathbf{p}} = -t_\epsilon(1 + e^{-i\mathbf{p}\cdot\mathbf{a}_1/\hbar} + e^{-i\mathbf{p}\cdot\mathbf{a}_2/\hbar}), \tag{2}$$

where $\mathbf{p} = (p_x, p_y)$ and t_ϵ is the nearest-neighbor hopping energy between an A and a B atom with the parametrization [23]: $\tan\varphi = \alpha \in [0, 1]$. In the position space, the primitive translation vectors are $\mathbf{a}_1 = a(\sqrt{3}/2, 3/2)$, $\mathbf{a}_2 = a(-\sqrt{3}/2, 3/2)$, where a is the lattice constant (intersite distance). The base vectors in the reciprocal lattice of the hexagonal Brillouin zone are $\mathbf{b}_1 = (\sqrt{3}/3, 1/3)2\pi/a$ and $\mathbf{b}_2 = (-\sqrt{3}/3, 1/3)2\pi/a$. The eigenenergy spectrum [23] of α-$\mathcal{T}_3$ lattice is independent of the value of α, which consists of a zero-energy flat band $E_0 = 0$ and two linearly dispersive bands $E_\lambda = \lambda|f_{\mathbf{p}}|$ with the band index $\lambda = \pm$. The structure of the positive band is shown in Fig. 1(b). There are two nonequivalent Dirac contact points: $+\mathbf{K} = (2/(3\sqrt{3}), 0)2\pi/a$ and $-\mathbf{K} = (-2/(3\sqrt{3}), 0)2\pi/a$.

Denoting the momentum vector from a Dirac point $\zeta\mathbf{K}$ as $\mathbf{q}$ and linearizing the corresponding function $f_{\mathbf{q}}$ in the Hamiltonian as

$$f_{\mathbf{q}} \approx v_F(\zeta q_x - iq_y), \tag{3}$$

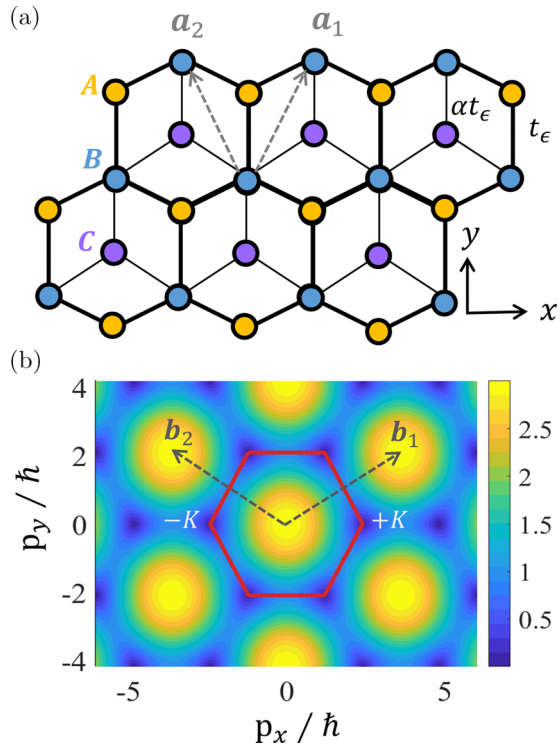

FIG. 1. Structure of α-$\mathcal{T}_3$ lattice and zero-field energy-band structure. (a) The lattice structure, where each unit cell contains three distinct atoms. The nearest-neighbor hopping energy between the A and B sites is t_ϵ and that between B and C sites is αt_ϵ. The material parameter α characterizes the relative coupling strength between the flat band and the Dirac-cone bands. (b) The zero-field energy spectrum of the positive dispersion band in the 2D momentum space for any α value, where the red hexagon denotes the first Brillouin zone and the zero-energy points give two topologically nonequivalent Dirac points $\zeta\mathbf{K}$ with the valley index $\zeta = \pm 1$.

where v_F is Fermi velocity, q_x, q_y are the momentum components measured from Dirac points with the valley index $\zeta = \pm 1$, we obtain the effective Hamiltonian in the continuum limit at low-energy excitation as

$$H_{\mathbf{q}} \approx v_F[\zeta S_x'(\varphi)q_x + S_y'(\varphi)q_y], \tag{4}$$

with

$$S_x'(\varphi) \equiv \begin{bmatrix} 0 & \cos\varphi & 0 \\ \cos\varphi & 0 & \sin\varphi \\ 0 & \sin\varphi & 0 \end{bmatrix}, \tag{5}$$

$$S_y'(\varphi) \equiv \begin{bmatrix} 0 & -i\cos\varphi & 0 \\ i\cos\varphi & 0 & -i\sin\varphi \\ 0 & i\sin\varphi & 0 \end{bmatrix}. \tag{6}$$

For $\alpha = 0$, $S_x'(0)$ and $S_y'(0)$ become $\sigma_x \oplus 0$ and $\sigma_y \oplus 0$, respectively, leading to

$$H_{\mathbf{q}}|_{\alpha=0} = v_F(\zeta\sigma_x q_x + \sigma_y q_y) \oplus 0, \tag{7}$$

$$H_{\text{spin-}\frac{1}{2}} = v_F(\sigma_x q_x + \sigma_y q_y). \tag{8}$$

For $\alpha = 1$, $S_x'(\pi/4)$ and $S_y'(\pi/4)$ are S_x and S_y, respectively, i.e., the components of the spin-1 matrix vector. In this case, we have

$$H_{\mathbf{q}}|_{\alpha=1} = v_F(\zeta S_x q_x + S_y q_y), \tag{9}$$

$$H_{\text{spin-1}} = v_F(S_x q_x + S_y q_y). \tag{10}$$

The continuum effective Hamiltonian of the α-$\mathcal{T}_3$ lattice, as given by Eq. (4), is a general model that includes the pseudospin-$\frac{1}{2}$ and pseudospin-1 lattices as the two opposite limiting cases. By varying the coupling strength $\alpha \in [0, 1]$, a continuous spectrum of Dirac-Weyl materials with a flat band can be generated.

B. Low-excitation continuum effective α-$\mathcal{T}_3$ Hamiltonian in a constant electric field

We apply a uniform and constant electric field to an α-$\mathcal{T}_3$ lattice in the x direction starting at time $t = 0$, represented by a time-dependent vector potential [31,50]. The corresponding continuum effective Hamiltonian around the two nonequivalent Dirac points becomes

$$H_{\mathbf{q}}(t) = v_F[\zeta S_x'(\varphi)q_x(t) + S_y'(\varphi)q_y], \tag{11}$$

with $q_x(t) \equiv q_x - e\mathcal{A}(t)$, where $\mathcal{A}(t) = \mathcal{E}t\Theta(t)$ and $\Theta(t)$ is a unit step function of time. The quantum dynamics are governed by

$$i\hbar\partial_t\psi_{\mathbf{q}}(t) = H_{\mathbf{q}}(t)\psi_{\mathbf{q}}(t). \tag{12}$$

In the Landau-Zener adiabatic basis [31,49], under an infinitesimal electric field, the evolution of a quantum state is transformed by

$$U_{\mathbf{q}}^\dagger(t)H_{\mathbf{q}}(t)U_{\mathbf{q}}(t) = S_z\varepsilon_{\mathbf{q}}(t), \tag{13}$$

where S_z is the z component of the spin-1 matrix vector and $U_{\mathbf{q}}(t)$ is given by

$$\begin{bmatrix} \frac{1}{\sqrt{2}}\cos\varphi\, e^{i\theta_{\mathbf{q}}} & \sin\varphi\, e^{i\theta_{\mathbf{q}}} & \frac{1}{\sqrt{2}}\cos\varphi\, e^{i\theta_{\mathbf{q}}} \\ \frac{1}{\sqrt{2}} & 0 & -\frac{1}{\sqrt{2}} \\ \frac{1}{\sqrt{2}}\sin\varphi\, e^{-i\theta_{\mathbf{q}}} & -\cos\varphi\, e^{-i\theta_{\mathbf{q}}} & \frac{1}{\sqrt{2}}\sin\varphi\, e^{-i\theta_{\mathbf{q}}} \end{bmatrix}, \tag{14}$$

with $\theta_{\mathbf{q}}(t)$ being the phase of $f_{\mathbf{q}}(t)$ and

$$\tan\theta_{\mathbf{q}}(t) = -\zeta q_y/[q_x - e\mathcal{A}(t)]$$

because of

$$f_{\mathbf{q}}(t) \approx v_F[\zeta q_x(t) - iq_y]. \tag{15}$$

The eigenstates of positive-, zero-, and negative-energy bands can then be written and be distinguished. For example, the positive-eigenenergy spectrum $\epsilon_{\mathbf{q}}(t) \equiv +|f_{\mathbf{q}}(t)|$ is given by

$$\varepsilon_{\mathbf{q}}(t) = v_F\sqrt{[q_x - e\mathcal{A}(t)]^2 + q_y^2}. \tag{16}$$

The transformed time-dependent Dirac equation becomes

$$i\hbar\partial_t\Phi_{\mathbf{q}}(t) = \left[S_z\varepsilon_{\mathbf{q}}(t) - \widetilde{S}_x\frac{\hbar v_F^2 q_y e\mathcal{E}}{\zeta\varepsilon_{\mathbf{q}}^2(t)}\right]\Phi_{\mathbf{q}}(t), \tag{17}$$

where

$$\Phi_{\mathbf{q}}(t) \equiv U_{\mathbf{q}}^{\dagger}(t)\psi_{\mathbf{q}}(t),$$
$$\widetilde{S}_x \equiv S_x \sin 2\varphi - S_L \cos 2\varphi,$$

with S_L defined by

$$S_L \equiv \begin{bmatrix} -1/2 & 0 & -1/2 \\ 0 & 1 & 0 \\ -1/2 & 0 & -1/2 \end{bmatrix}. \tag{18}$$

The second term in Eq. (17) arises from the time dependence of the unitary transformation $-i\hbar U_{\mathbf{q}}^{\dagger}(t)\partial_t U_{\mathbf{q}}(t)$. Consider the initial state in which the lower Dirac cone is fully occupied:

$$\Phi_{\mathbf{q}}(t=0) = [0, 0, 1]^T, \tag{19}$$

the average current density $\langle \mathcal{J}_x \rangle_{\mathbf{q}}(t)$ in the momentum space is invariant under the unitary transformation:

$$\begin{aligned}\langle \mathcal{J}_x \rangle_{\mathbf{q}}(t) &\equiv -e[\psi_{\mathbf{q}}(t)]^{\dagger}(\partial_{q_x(t)} H_{\mathbf{q}}(t))\psi_{\mathbf{q}}(t), \\ &= -ev_F\zeta\ \Phi_{\mathbf{q}}^{\dagger}(t)[U_{\mathbf{q}}^{\dagger}(t)S_x'(\varphi)U_{\mathbf{q}}(t)]\Phi_{\mathbf{q}}(t). \end{aligned}\tag{20}$$

In the adiabatic basis, $\Phi_{\mathbf{q}}(t)$ can be expressed as

$$\Phi_{\mathbf{q}}(t) = [\xi_{\mathbf{q}}(t), \quad \gamma_{\mathbf{q}}(t), \quad \beta_{\mathbf{q}}(t)]^T, \tag{21}$$

where $|\xi_{\mathbf{q}}|^2$, $|\gamma_{\mathbf{q}}|^2$, and $|\beta_{\mathbf{q}}|^2$ are the probabilities of finding the quasiparticle in the upper, flat, and lower band, respectively. The average current density can be decomposed into two parts [31],

$$\langle \mathcal{J}_x \rangle_{\mathbf{q}}(t) = \langle \mathcal{J}_x \rangle_{\mathbf{q}}^{\text{intra}}(t) + \langle \mathcal{J}_x \rangle_{\mathbf{q}}^{\text{inter}}(t), \tag{22}$$

which are the intraband and interband currents, respectively, given by

$$\langle \mathcal{J}_x \rangle_{\mathbf{q}}^{\text{intra}}(t) = -ev_F\zeta \cos[\theta_{\mathbf{q}}(t)](|\xi_{\mathbf{q}}(t)|^2 - |\beta_{\mathbf{q}}(t)|^2), \tag{23}$$

$$\begin{aligned}\langle \mathcal{J}_x \rangle_{\mathbf{q}}^{\text{inter}}(t) = -ev_F\zeta\ &\sin[\theta_{\mathbf{q}}(t)](2\cos[2\varphi]\ \text{Re}[i\xi_{\mathbf{q}}^*(t)\beta_{\mathbf{q}}(t)] \\ &+ \sqrt{2}\sin[2\varphi]\ \text{Re}[i\xi_{\mathbf{q}}^*(t)\gamma_{\mathbf{q}}(t) + i\gamma_{\mathbf{q}}^*(t)\beta_{\mathbf{q}}(t)]), \end{aligned}\tag{24}$$

with

$$\sin[2\varphi] = 2\alpha/(1+\alpha^2),$$
$$\cos[2\varphi] = (1-\alpha^2)/(1+\alpha^2).$$

The intraband component represents the current density of the electrons and holes in the upper and lower band, respectively, with the opposite signs. The interband component depicts the current density due to the interference between the upper, flat, and lower bands, where the material parameter α modulates contributions to the current density from the coupling between energy bands. In particular, for $\alpha = 0$, the only contribution to the current is the transition from the lower to the upper band. However, for $\alpha = 1$, the current density is due to the coupling between the flat band and the other bands. For $\alpha \in (0, 1)$, the interband current density is a mixture of the two extreme cases.

Using the normalization condition, we have

$$|\xi_{\mathbf{q}}(t)|^2 - |\beta_{\mathbf{q}}(t)|^2 = 2|\xi_{\mathbf{q}}(t)|^2 + |\gamma_{\mathbf{q}}(t)|^2 - 1. \tag{25}$$

Substituting Eq. (25) into the intraband current in Eq. (23), we have that the constant in the third term of Eq. (25) vanishes [31] after a momentum integration. Theoretically, the integration region is infinite over the momentum space from a Dirac point ζK. From Eq. (23), the integrand is a periodic function: $\cos[\theta_q(t)]$, whose integration over an infinite region is zero. The intraband current is then the contribution from the flat and upper bands. More specifically, we denote $\mathcal{J}^{\text{intra}}(t)$ and $\mathcal{J}^{\text{inter}}(t)$ as the momentum integration of $\langle \mathcal{J}_x \rangle_{\mathbf{q}}^{\text{intra}}(t)$ and $\langle \mathcal{J}_x \rangle_{\mathbf{q}}^{\text{inter}}(t)$, respectively. Since numerical integration cannot be done in the infinite-momentum space from a Dirac point, we limit the integration region in the continuum model to a finite-momentum region to ensure the convergence of the current: $\mathcal{J}(t) = \mathcal{J}^{\text{intra}}(t) + \mathcal{J}^{\text{inter}}(t)$. It is worth noting that the effective model described by Eq. (11) is derived using a Taylor expansion about a single Dirac point, so the integration of the average current density from the effective Hamiltonian includes contributions from this Dirac point only. We can decompose the contributions from all the energy bands in the intraband and interband currents by integrating Eqs. (23) and (24) over the momentum space and following the term order in Eqs. (23) and (24) to define

$$\begin{aligned}\mathcal{J}^{\text{intra}}(t) &= \mathcal{J}_{\xi}^{\text{intra}}(t) + \mathcal{J}_{\gamma}^{\text{intra}}(t), \\ \mathcal{J}^{\text{inter}}(t) &= \mathcal{J}_{\xi\beta}^{\text{inter}}(t) + \mathcal{J}_{\xi\gamma}^{\text{inter}}(t) + \mathcal{J}_{\gamma\beta}^{\text{inter}}(t). \end{aligned}\tag{26}$$

These expressions are convenient for treating the contributions to the current by the multiple energy bands in the weak field (Sec. III A) and strong field (Sec. III B) cases.

To streamline numerical calculations, we define a number of dimensionless physical quantities in the continuum effective α-$\mathcal{T}_3$ model:

$$\begin{aligned}\widetilde{t} &= t/t_0, \\ \widetilde{q}_x &= q_x/q_0, \\ \widetilde{q}_y &= q_y/q_0, \\ \widetilde{\mathcal{E}} &= \mathcal{E}/\mathcal{E}_0, \\ \widetilde{\varepsilon}_q(t) &= \varepsilon_q(t)/\varepsilon_0, \\ \widetilde{\mathcal{J}}(t) &= \mathcal{J}(t)/\mathcal{J}_0, \\ \langle \widetilde{\mathcal{J}}_x \rangle_q(t) &= \langle \mathcal{J}_x \rangle_{\mathbf{q}}(t)/\langle \mathcal{J}_0 \rangle_{\mathbf{q}}, \end{aligned}\tag{27}$$

where $t_0 \equiv \hbar/t_\epsilon$, $q_0 \equiv t_\epsilon/v_F$, $\mathcal{E}_0 \equiv t_\epsilon^2/(e\hbar v_F)$, $\varepsilon_0 \equiv t_\epsilon$,

$$\mathcal{J}_0 \equiv e^2\mathcal{E}_0/\hbar \sim ev_F/a^2,$$

and $\langle \mathcal{J}_0 \rangle_{\mathbf{q}} \equiv ev_F$.

C. General α-$\mathcal{T}_3$ lattice Hamiltonian in a constant electric field

With a constant electric field switched on at $t = 0$ in the x direction, the x component of the momentum is $p_x(t) \equiv p_x - eEt$. The general Hamiltonian of the α-$\mathcal{T}_3$ lattice is given by

$$H(t) = \begin{bmatrix} 0 & f_{\mathbf{p}}(t)\cos\varphi & 0 \\ f_{\mathbf{p}}^*(t)\cos\varphi & 0 & f_{\mathbf{p}}(t)\sin\varphi \\ 0 & f_{\mathbf{p}}^*(t)\sin\varphi & 0 \end{bmatrix}, \tag{28}$$

where

$$f_{\mathbf{p}}(t) = -t_\epsilon\left[1 + 2\,\exp\left(-i\frac{3}{2}\frac{p_y a}{\hbar}\right)\cos\left(\frac{\sqrt{3}}{2}\frac{p_x(t)a}{\hbar}\right)\right]. \tag{29}$$

The eigenenergy spectrum of the flat band is $\varepsilon_0 = 0$, and the positive dispersion band in the whole hexagonal Brillouin zone is determined by $\varepsilon_{\mathbf{p}}(t) = +|f_{\mathbf{p}}(t)|$:

$$\varepsilon_{\mathbf{p}}(t) = t_\epsilon\sqrt{1 + 4\,\cos X_{\mathbf{p}}(t)[\cos Y_{\mathbf{p}} + \cos X_{\mathbf{p}}(t)]}, \tag{30}$$

where $X_{\mathbf{p}}(t) = \sqrt{3}p_x(t)a/(2\hbar)$ and $Y_{\mathbf{p}} = 3p_y a/(2\hbar)$. The unitary transformation $U_{\mathbf{p}}(t)$ is similar to that in Eq. (14) except that $\theta_{\mathbf{q}}(t)$ is now replaced by $\theta_{\mathbf{p}}(t)$, which is the phase of $f_{\mathbf{p}}(t)$ in Eq. (29). The transformed quantum dynamics are governed by [40]

$$i\hbar\partial_t\Phi_{\mathbf{p}}(t) = \left[S_z\varepsilon_{\mathbf{p}}(t) - \widetilde{S}_x\frac{at_\epsilon^2 eE}{\varepsilon_{\mathbf{p}}^2(t)}C_{\mathbf{p}}(t)\right]\Phi_{\mathbf{p}}(t), \tag{31}$$

with the coefficient given by

$$C_{\mathbf{p}}(t) = \sqrt{3}\,\sin Y_{\mathbf{p}}\sin X_{\mathbf{p}}(t).$$

The average current density $\langle J_x\rangle_{\mathbf{p}}(t)$ contains two contributions: interband and intraband transitions [31], which can generally be written as [40]

$$\langle J_x\rangle_{\mathbf{p}}^{\text{intra}}(t) = J_{x,\mathbf{p}}^{11}(t)(|\xi_{\mathbf{p}}(t)|^2 - |\beta_{\mathbf{p}}(t)|^2), \tag{32}$$

$$\begin{aligned}\langle J_x\rangle_{\mathbf{p}}^{\text{inter}}(t) = {}& 2\,\text{Re}\big[J_{x,\mathbf{p}}^{13}(t)\xi_{\mathbf{p}}^*(t)\beta_{\mathbf{p}}(t)\big]\\ &+ 2\,\text{Re}\big[J_{x,\mathbf{p}}^{12}(t)\xi_{\mathbf{p}}^*(t)\gamma_{\mathbf{p}}(t) + J_{x,\mathbf{p}}^{23}(t)\gamma_{\mathbf{p}}^*(t)\beta_{\mathbf{p}}(t)\big].\end{aligned} \tag{33}$$

To gain insights into these contributions to the average current density $\langle J_x\rangle_{\mathbf{p}}(t)$, we recall the matrix of the current density operator:

$$J_{x,\mathbf{p}}(t) = -eU_{\mathbf{p}}^\dagger(t)\partial_{p_x(t)}H(t)U_{\mathbf{p}}(t).$$

The intraband contribution is made by both electrons and holes, corresponding to

$$\begin{aligned}J_{x,\mathbf{p}}^{11}(t) &\equiv J_{x,\mathbf{p}}^{0}(t)\cos\Theta_{\mathbf{p}}(t),\\ J_{x,\mathbf{p}}^{33}(t) &= -J_{x,\mathbf{p}}^{11}(t),\end{aligned}$$

respectively. The interband contribution arises from the interference of the transitions from the lower to the flat band or the upper band and from the flat to the upper band, corresponding to $J_{x,\mathbf{p}}^{23}(t)$, $J_{x,\mathbf{p}}^{13}(t)$, and $J_{x,\mathbf{p}}^{12}(t)$, respectively, which are given by

$$\begin{aligned}J_{x,\mathbf{p}}^{13}(t) &\equiv iJ_{x,\mathbf{p}}^{0}(t)\cos[2\varphi]\ \sin[\Theta_{\mathbf{p}}(t)],\\ J_{x,\mathbf{p}}^{12}(t) &\equiv iJ_{x,\mathbf{p}}^{0}(t)\sin[2\varphi]\sin[\Theta_{\mathbf{p}}(t)]/\sqrt{2},\\ J_{x,\mathbf{p}}^{23}(t) &= J_{x,\mathbf{p}}^{12}(t),\end{aligned} \tag{34}$$

where $\Theta_{\mathbf{p}}(t) \equiv \theta_{\mathbf{p}}(t) + Y_p$ and $J_{x,\mathbf{p}}^{0}(t)$ is the common factor with the dimension of the current density:

$$J_{x,\mathbf{p}}^{0}(t) = -\sqrt{3}\,\sin[X_{\mathbf{p}}(t)]eat_\epsilon/\hbar.$$

We use $J(t)$ to denote the integration of $\langle J_x\rangle_{\mathbf{p}}(t)$ in the first Brillouin zone, which will be used to characterize the Bloch oscillations (in Sec. III C).

For the general α-$\mathcal{T}_3$ lattice calculations, the following dimensionless quantities are convenient:

$$\begin{aligned}\widetilde{p}_x &= p_x/p_0,\\ \widetilde{p}_y &= p_y/p_0,\\ \widetilde{E} &= E/E_0,\\ \widetilde{J}(t) &= J(t)/J_0,\\ \langle\widetilde{J}_x\rangle_{\mathbf{p}}(t) &= \langle J_x\rangle_{\mathbf{p}}(t)/\langle J_0\rangle_{\mathbf{p}},\end{aligned} \tag{35}$$

with $p_0 \equiv \hbar/a$, $E_0 \equiv t_\epsilon/(ea)$, $J_0 = e^2E_0/\hbar \sim et_\epsilon/(\hbar a)$, and $\langle J_0\rangle_{\mathbf{p}} = eat_\epsilon/\hbar$.

D. Calculating the Berry phases of the α-$\mathcal{T}_3$ lattice

The Berry phases associated with the conical and flat bands can be calculated by assuming that the corresponding eigenstates adiabatically evolve with time along an arbitrarily closed loop around the Dirac points $\zeta\mathbf{K}$ in the momentum space [8]:

$$\phi_{n,\zeta} = \frac{-i}{\pi}\oint dp\cdot\langle\psi_n|\nabla_{\mathbf{p}}|\psi_n\rangle, \tag{36}$$

which can be calculated either by the continuum effective Hamiltonian or by the general lattice Hamiltonian (both giving the same results). For example, from the general lattice model, the eigenstate of the flat band is

$$|\psi_0\rangle = \begin{bmatrix}\sin\varphi\ e^{i\theta_{\mathbf{p}}}\\ 0\\ -\cos\varphi\ e^{-i\theta_{\mathbf{p}}}\end{bmatrix}, \tag{37}$$

and the eigenstates of the conduction and valence bands with $\lambda = \pm 1$, respectively, are

$$|\psi_\lambda\rangle = \frac{1}{\sqrt{2}}\begin{bmatrix}\cos\varphi\ e^{i\theta_{\mathbf{p}}}\\ \lambda\\ \sin\varphi\ e^{-i\theta_{\mathbf{p}}}\end{bmatrix}, \tag{38}$$

where $\theta_{\mathbf{p}}$ is the phase of the $f_{\mathbf{p}}$ in Eq. (2). The eigenstates in the continuum effective model are similar to those in the general lattice model except that $\theta_{\mathbf{p}}$ is replaced by $\theta_{\mathbf{q}}$, the phase of the $f_{\mathbf{q}}$ in Eq. (3). The Berry phases of the dispersive conical bands and the dispersionless flat band are given by [8,23]

$$\phi_{\lambda,\zeta} = \pi\zeta\ \cos 2\varphi = \pi\zeta\left(\frac{1-\alpha^2}{1+\alpha^2}\right), \tag{39}$$

$$\phi_{0,\zeta} = -2\pi\zeta\ \cos 2\varphi = -2\pi\zeta\left(\frac{1-\alpha^2}{1+\alpha^2}\right), \tag{40}$$

respectively. Note that the Berry phases are topological but not π quantized [23] and are distinct in the $+\mathbf{K}$ and $-\mathbf{K}$ valleys except for $\alpha = 0, 1$. Figure 2 shows that the Berry phase is a monotonic function of the material parameter α. The average current density in Eqs. (23), (24), (32), and (33) also depends on α. If this dependence is monotonic, there will be a one-to-one correspondence between the current and the Berry phases, providing a mechanism to determine the Berry phases by measuring the current.

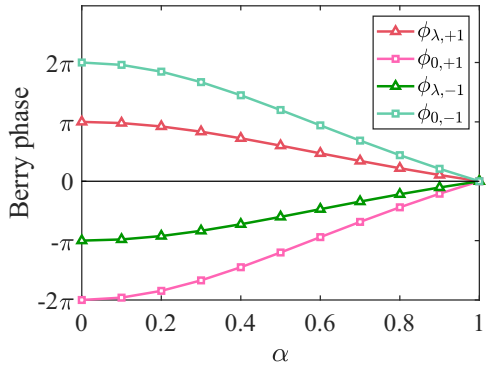

FIG. 2. Berry phases of orbits in different energy bands around the Dirac points $\pm\mathbf{K}$ versus the material parameter α. The dependence of the Berry phases on α is monotonic.

III. BALLISTIC TRANSPORT AND BERRY PHASE DETECTION

For nonequilibrium quantum transport in the α-$\mathcal{T}_3$ lattice at zero temperature, depending on the timescale of ballistic transport, distinct physical behaviors can arise. First, in the presence of a uniform electric field, if its product with time is comparable to the quantity $\hbar/(ea)$: $Et_{\rm Bloch} \sim \hbar/(ea)$, the average current density will undergo Bloch oscillations [35,36] due to the Bloch band in the periodic Brillouin zone. If, on this timescale, two levels do not cross each other, Landau-Zener transition will occur, leading to Bloch-Zener oscillations [40]. Second, if the timescale is much shorter than the Bloch time $t \ll t_{\rm Bloch}$, the lattice can effectively be described by the continuum effective α-$\mathcal{T}_3$ Hamiltonian. Third, when the timescale is in the Schwinger regime

$$\sqrt{\hbar/(v_F e\mathcal{E})} \ll t \ll t_{\rm Bloch},$$

the transport process becomes nonlinear: $\mathcal{J} \propto t\mathcal{E}^{3/2}$. Fourth, when the timescale continues to reduce to the Kubo regime

$$h/W \ll t \ll \sqrt{\hbar/(v_F e\mathcal{E})},$$

where W is the bandwidth, the average electric current density is saturated and independent of time: $\mathcal{J} \propto \mathcal{E}$. Finally, for the ultrashort time transient response $t \ll h/W$, the current behavior becomes full classical $\mathcal{J} \propto \mathcal{E}t$.

To describe our results unambiguously, it is necessary to distinguish the electric field and current in the two cases where the α-$\mathcal{T}_3$ material is described by the effective continuum model and by the general lattice model. We use $\mathcal{E}$ and $\mathcal{J}$ to denote the electric field and current in the former, while E and J in the latter.

A. Kubo regime

In the Kubo regime of the weak electric field, we have

$$|\mathbf{q}| = \sqrt{q_x^2 + q_y^2} \gg e\mathcal{E}t, \tag{41}$$

for $|\mathbf{q}| \neq 0$ (not too close to the Dirac points). In Eq. (17), the term $e\mathcal{E}t$ in $\varepsilon_{\mathbf{q}}(t)$ can then be neglected but the field term in the numerator term $-i\hbar U_{\mathbf{q}}^{\dagger}(t)\partial_t U_{\mathbf{q}}(t)$ should be retained. Initially, at $t = 0$, all electrons stay in the lower-energy band. For $t > 0$, a uniform constant electric field is switched on along the x direction, and electron-positron pairs are created by the Schwinger mechanism [31,32] in the continuum effective model. Since only a small number of the particles are excited, the interband (or polarization) contribution from the interference between the energy bands dominates over the intraband (or conduction) contribution. In this regime, *Zitterbewegung* governs the small field linear response, where all electrons propagate with the maximal velocity v_F, leading to a saturated current independent of time.

Integrating the average current density associated with the momentum $\langle\mathcal{J}_x\rangle_{\mathbf{q}}^{\rm inter}(t)$ over the whole momentum space gives

$$\mathcal{J}^{\rm inter} \equiv \langle\mathcal{J}_x\rangle^{\rm inter} = \frac{1}{\pi^2\hbar^2}\int_0^{\infty} q\,dq \int_0^{2\pi} d\varphi\ \langle\mathcal{J}_x\rangle_{\mathbf{q}}^{\rm inter}(t), \tag{42}$$

where q and φ are the radial and angular variables in momentum space, respectively. For pseudospin-$\frac{1}{2}$ quasiparticles ($\alpha = 0$), the linear scaling law for the current is [31]

$$\mathcal{J}_{\text{spin-1/2}}^{\rm inter} = e^2\mathcal{E}/(4\hbar)$$

with the dimensionless relation

$$\widetilde{\mathcal{J}}_{\text{spin-1/2}}^{\rm inter} = \tfrac{1}{4}\widetilde{\mathcal{E}}. \tag{43}$$

For pseudospin-1 quasiparticles ($\alpha = 1$), due to the flat band, the current saturation value is amplified by a factor of 2 and the corresponding linear scaling law becomes [50]

$$\widetilde{\mathcal{J}}_{\text{spin-1}}^{\rm inter} = \tfrac{1}{2}\widetilde{\mathcal{E}}. \tag{44}$$

For $0 < \alpha < 1$, the saturated value of the current over the electric field $\widetilde{\mathcal{J}}^{\rm inter}/\widetilde{\mathcal{E}}$ is between $\frac{1}{4}$ and $\frac{1}{2}$, as shown in Fig. 3, where the current is normalized by the constant $\frac{1}{4}$.

On the ultrashort timescale, the current exhibits a fully classical behavior: $\widetilde{\mathcal{J}}/\widetilde{\mathcal{E}} \propto \widetilde{t}$. After a certain time, the current saturates. We tune the material parameter α to assess the interplay between the flat band and the saturated current in the weak field regime. For $\alpha = 0$, there is zero coupling between the flat and the two dispersive bands, so the interband current is solely determined by the interference between the lower and the upper conical bands as $\widetilde{\mathcal{J}}_{\xi\beta}^{\rm inter}$. For the opposite extreme case of $\alpha = 1$, the saturated current is the result of the interference between the lower and the flat band: $\widetilde{\mathcal{J}}_{\gamma\beta}^{\rm inter}$. For $0 < \alpha < 1$, the total interband saturated current is a mixture of the interference contributions between $\widetilde{\mathcal{J}}_{\xi\beta}^{\rm inter}$ and $\widetilde{\mathcal{J}}_{\gamma\beta}^{\rm inter}$, as shown in Fig. 3. Note that the interference between the flat and the upper bands does not directly contribute any current for the entire α spectrum because the combination of the interference between the lower and flat bands and that between the flat and upper bands is physically equivalent to the interference between the lower and upper bands.

As α increases from zero, the saturated current from the interference between the lower and upper bands decreases, and the current from the interference between the lower and the flat band increases, as shown in Fig. 4(a). In the regime of weak field, the flat band suppresses the current from the interference between the lower and upper bands, and enhances the one from the interference between the lower and flat bands for $\alpha \in (0, 1)$, as shown in Fig. 4(b). In this case, detecting the Berry phase through the current probe is feasible since there

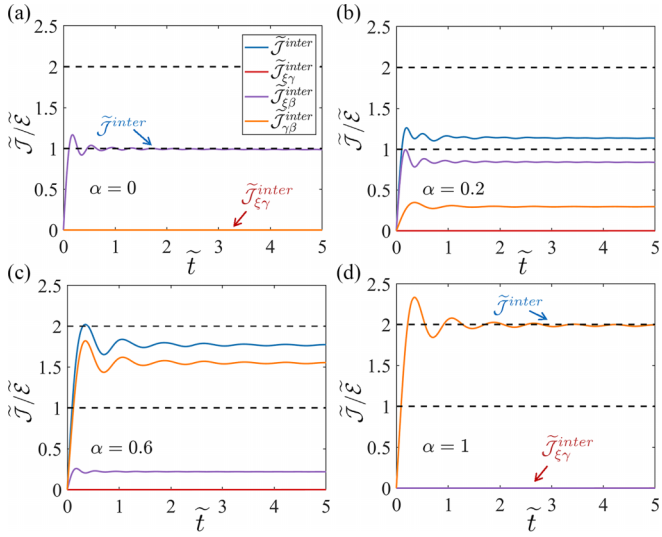

FIG. 3. Time evolution of the current from the effective continuum Hamiltonian in the Kubo regime. Shown is the interband current divided by the electric field: $\widetilde{\mathcal{J}}/\widetilde{\mathcal{E}}$ for $0 \leqslant \alpha \leqslant 1$. (a)–(d) Saturated currents divided by the electric field: $\widetilde{\mathcal{J}}/\widetilde{\mathcal{E}}$, for the total interband current $\widetilde{\mathcal{J}}^{\text{inter}}$, the interference current between the flat and the upper band $\widetilde{\mathcal{J}}^{\text{inter}}_{\xi\gamma}$, the current between the lower and the upper band $\widetilde{\mathcal{J}}^{\text{inter}}_{\xi\beta}$, and that between the lower and the flat band $\widetilde{\mathcal{J}}^{\text{inter}}_{\gamma\beta}$ for $\alpha = 0,\ 0.2,\ 0.6,\ 1$, respectively. For comparison, all currents are divided by $\frac{1}{4}$. Other parameters are electric field $\widetilde{\mathcal{E}} = 0.0004$, valley index of the Dirac point $\zeta = +1$, size of momentum space in $\widetilde{q}_x, \widetilde{q}_y \in [-8, 8]$, and step sizes of momentum and time $d\widetilde{q} = d\widetilde{t} = 0.01$. Note the cut width about the Dirac point is $\widetilde{q}_{\text{cut}} = 0.005$ in the momentum space to make valid the weak field approximation and the quantum dynamic equation (17).

is a one-to-one correspondence between the saturated current value and the Berry phase, as shown in Figs. 2 and 4(a).

B. Schwinger regime

Under a strong electric field

$$(q_x, eEt - q_x) \gg |q_y|, \tag{45}$$

the α-$\mathcal{T}_3$ lattice system is in the Schwinger regime. In this regime, electrons are excited from the lower band to the flat and upper bands via the Schwinger mechanism, where the electric field in the vacuum decays and loses energy due to the production of the electron-positron pairs. The transition probability to the flat or upper band is the same as the Landau-Zener transition probability, where the finite-energy gap between the two avoided-crossing levels induces the nonadiabatic Landau-Zener transition driven by the electric field. In the general α-$\mathcal{T}_3$ lattice or the corresponding continuum model, Landau-Zener transitions occur in the neighborhood of the Dirac points [40] because the energy gap is comparable with that given by the magnitude of the electric field. After the Landau-Zener transition, the quantum states are superposition of the states associated with the three levels [40], and the nonzero component of the occupied probability in the flat band is a manifestation of the Landau-Zener transition from the lower band to the flat band. This transition leaves more holes in the lower band, leading to an increase in the current.

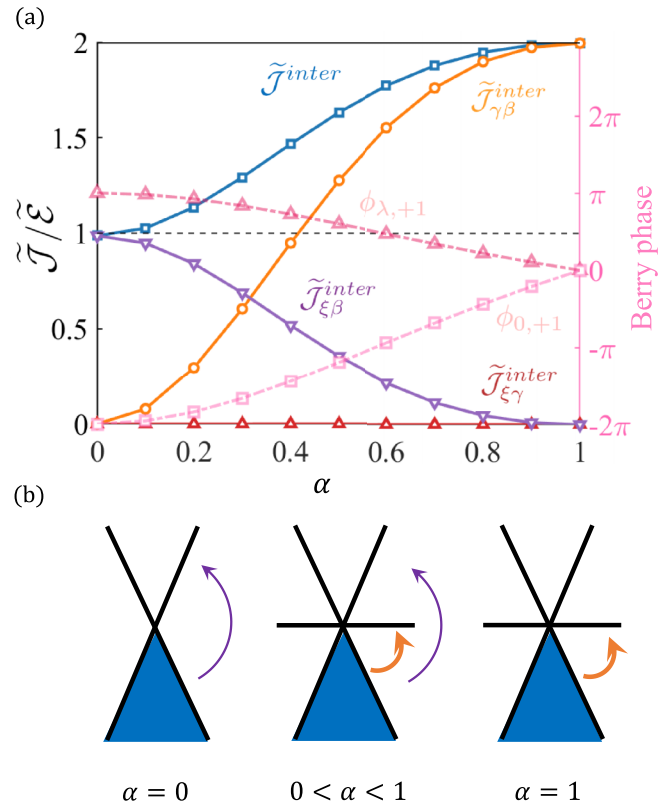

FIG. 4. Flat-band contribution to the saturated current in the Kubo regime. (a) Corresponding to the Berry phase diagram in Fig. 2, the saturated current (the current at the end of time evolution in Fig. 3) changes with the materials parameter α for the total interband contribution $\widetilde{\mathcal{J}}^{\text{inter}}$, the interference current between the flat and upper bands $\widetilde{\mathcal{J}}^{\text{inter}}_{\xi\gamma}$, the current between the lower and upper bands $\widetilde{\mathcal{J}}^{\text{inter}}_{\xi\beta}$, and that between the lower and flat bands $\widetilde{\mathcal{J}}^{\text{inter}}_{\gamma\beta}$. (b) A schematic display of the mixing process of interference between the lower and upper bands and that between the lower and flat bands for $\alpha \in (0, 1)$.

Specifically, in the Schwinger regime, the electric current is dominated by the intraband transitions, including the flat-band contribution. The flat band is dispersionless because it has zero group velocity for the wave packets. This means that the wave packets corresponding to the flat band are localized in the real space. However, the flat band also contributes to the intraband current even though its group velocity is zero, for the following reasons. First, both electrons and holes contribute to the current. Second, a Landau-Zener transition from the lower to the flat band can create relatively more holes, giving rise to an extra current compared to the case without a flat band. As a result, the intraband current is proportional to the number of excited particles in both the flat and upper bands.

Integrating the current $\langle \mathcal{J}_x \rangle^{\text{intra}}_{\mathbf{q}}(t)$ over the whole momentum space gives

$$\begin{aligned} \mathcal{J}^{\text{intra}}(t) &\equiv \langle \mathcal{J}_x \rangle^{\text{intra}}(t) \\ &= \frac{1}{\pi^2 \hbar^2} \int_0^{\infty} q\, dq \int_0^{2\pi} d\varphi\ \langle \mathcal{J}_x \rangle^{\text{intra}}_{\mathbf{q}}(t), \end{aligned} \tag{46}$$

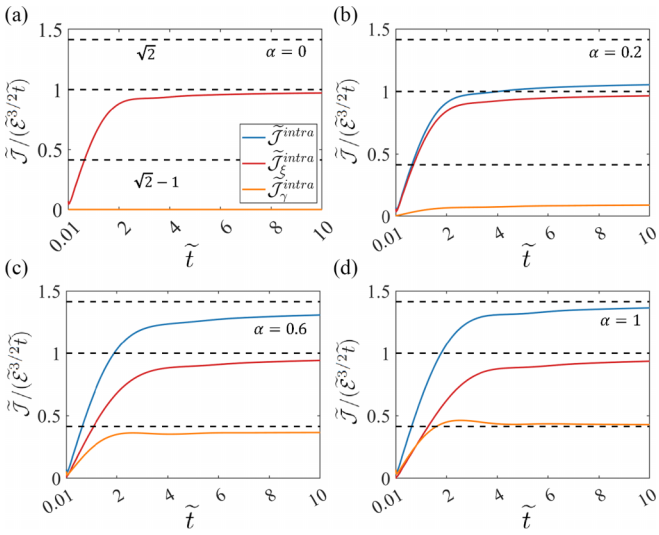

FIG. 5. Time evolution of the normalized intraband current from the continuum effective model in the Schwinger regime. The quantity displayed is $\widetilde{\mathcal{J}}/(\widetilde{\mathcal{E}}^{3/2}\widetilde{t})$. (a)–(d) The total intraband saturated current $\widetilde{\mathcal{J}}^{\rm intra}$ from the upper band current $\widetilde{\mathcal{J}}^{\rm intra}_{\xi}$ and the flat-band current $\widetilde{\mathcal{J}}^{\rm intra}_{\gamma}$ for $\alpha = 0,\ 0.2,\ 0.6,\ 1$, respectively. For comparison, all currents are divided by $2/\pi^2$. Other parameters are electric field $\widetilde{\mathcal{E}} = 0.4096$, valley index $\zeta = +1$, size of momentum space $\widetilde{q}_x, \widetilde{q}_y \in [-8, 8]$, and step sizes of momentum and time $d\widetilde{q} = d\widetilde{t} = 0.01$. The width of the region in the momentum space about the Dirac point in which the continuum effective Hamiltonian holds is $\widetilde{q}_{\rm cut} = 0.0001$.

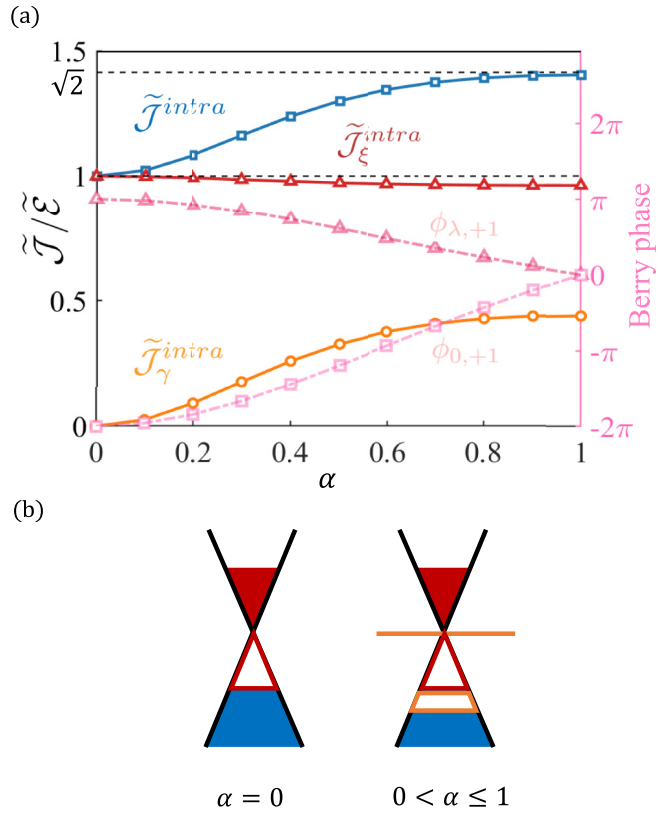

FIG. 6. Flat band contributions to the saturated current in the Schwinger regime. (a) Corresponding to the Berry phase diagram in Fig. 2, the saturated current (at the end of the time evolution in Fig. 5) varies with the material parameter α for the total intraband current density $\widetilde{\mathcal{J}}^{\rm intra}$, the upper band current $\widetilde{\mathcal{J}}^{\rm intra}_{\xi}$, and the flat band current $\widetilde{\mathcal{J}}^{\rm intra}_{\gamma}$ for $0 \leqslant \alpha \leqslant 1$. (b) A schematic illustration of the electron-hole excitation and the extra holes from the flat band in comparison with the graphene case. The flat band, despite its zero group velocity, has the ability to enhance the electric current.

with q and φ being the radial and angular variables in momentum space, respectively. This form is similar in mathematical form to that of the interband case. However, a key difference is that the time-dependent intraband current displays a nonlinear response. For pseudospin-$\frac{1}{2}$ Dirac particles, the dimensionless form of the intraband current is given by [31]

$$\widetilde{\mathcal{J}}^{\rm intra}_{\text{spin-1/2}}(\widetilde{t}) = \frac{2}{\pi^2}\widetilde{\mathcal{E}}^{3/2}\widetilde{t}. \tag{47}$$

For pseudospin-1 Dirac-Weyl particles, the intraband current is [50]

$$\widetilde{\mathcal{J}}^{\rm intra}_{\text{spin-1}}(\widetilde{t}) = \frac{2\sqrt{2}}{\pi^2}\widetilde{\mathcal{E}}^{3/2}\widetilde{t}, \tag{48}$$

where the flat-band contribution is

$$\widetilde{\mathcal{J}}^{\rm intra}_{\rm flat}(\widetilde{t}) = \frac{2(\sqrt{2}-1)}{\pi^2}\widetilde{\mathcal{E}}^{3/2}\widetilde{t}. \tag{49}$$

The continuum effective α-$\mathcal{T}_3$ Hamiltonian can be used to gain insights into the origin of the intraband current in the Schwinger regime. For $\alpha = 0$ with pseudospin-$\frac{1}{2}$ Dirac particles, there is no coupling between the flat band and the two conical dispersive bands, so the only excitation is one from the lower to the upper band. The intraband current depends only on the Landau-Zener transition to the upper band, as illustrated in Fig. 5(a).

Graphene can serve as a benchmark for comparison with the general $\alpha > 0$ cases. For the opposite extreme case of $\alpha = 1$ with pseudospin-1 Dirac-Weyl particles, the quantity $\widetilde{\mathcal{J}}/(\widetilde{\mathcal{E}}^{3/2}\widetilde{t})$ of the upper band is in principle the same as that for the $\alpha = 0$ case, with the current from the Landau-Zener transition to the flat band converging to the constant $\sqrt{2}-1$, as shown in Fig. 5(d). For $0 < \alpha < 1$, the intraband current of the upper band is approximately constant and flat-band current is enhanced with increasing α, as shown in Figs. 5(a)–5(d) and 6(a). In the Schwinger regime, the flat band contributes extra holes with positive charges, thereby enhancing the intraband current by the factor of $\sqrt{2}$ compared with the graphene benchmark, as schematically illustrated in Fig. 6(b). Since the converged intraband current depends monotonically on the materials parameter α, it can be exploited to assess the Berry phase.

In the Schwinger regime, the total difference in the prefactor of the intraband current between pseudospin-$\frac{1}{2}$ and pseudospin-1 Dirac-Weyl particles from Eqs. (47) and (48), respectively, arises from the Landau-Zener transitions. The results in Eqs. (47) and (48) have a difference of $\sqrt{2}$ in the prefactor. Since the 2×2 spin-$\frac{1}{2}$ and the 3×3 spin-1 matrices differ by a prefactor of $1/\sqrt{2}$, could this be the reason for the perfactor difference in the current? To answer this question, we note that, mathematically, in the effective Hamiltonian, the intraband current $\mathcal{J}^{\rm intra}(t)$ is in principle the integration of the average intraband current density over the infinite-momentum

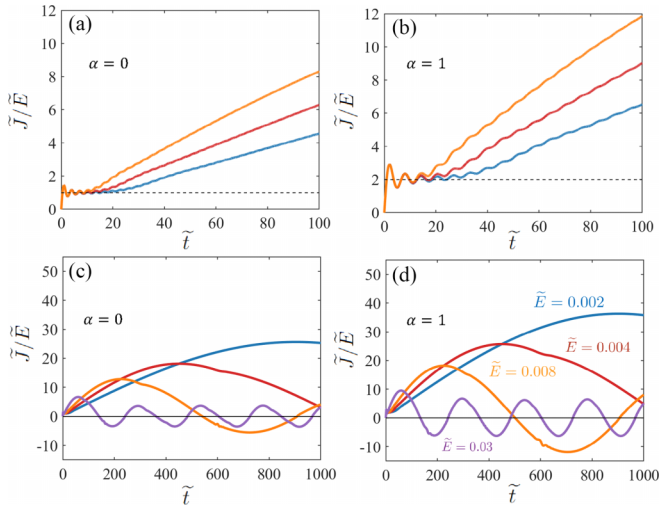

FIG. 7. Time evolution of the total current (interband and intraband) calculated from the general α-$\mathcal{T}_3$ lattice model. The quantity displayed is $\widetilde{J}/\widetilde{E}$. (a), (b) Ultrashort time transient response as well as the linear and nonlinear responses for $\widetilde{E} = 0.002,\ 0.004,\ 0.008$ and for $\alpha = 0,\ 1$, respectively. For comparison, all currents are divided by $\frac{1}{4}$, the saturated value of the weak field for graphene, and a factor of 2 due to the momentum integration region being the first hexagonal Brillouin zone that contains two nonequivalent Dirac points. (c), (d) Bloch-Zener oscillations for $\alpha = 0,\ 1$, respectively, for different electric fields. Relevant parameter values are time-step size $d\widetilde{t} = 0.01$, momentum-step size $d\widetilde{p}_x = d\widetilde{p}_y = 0.002$, width around the Dirac point $\widetilde{p}_{\rm cut} = 0.001$ in the momentum space.

space $\langle \mathcal{J}_x \rangle_{\mathbf{q}}^{\rm intra}(t)$, as given by Eq. (46). In the Schwinger regime, the intraband contribution dominates, so the interband current effect can be neglected. The total average current density $\langle \mathcal{J}_x \rangle_{\mathbf{q}}(t)$ is obtained from the original Hamiltonian in Eq. (20). From this formula, we see that the current contribution depends not only on the spin matrix $S'_x(\varphi)$ but also on the intrinsic dynamical evolution of the wave function $\psi_{\mathbf{q}}(t)$. Furthermore, the derived intraband average current density is given by Eq. (23), which does not provide explicit evidence that the current depends solely on the spin matrices.

C. Bloch-Zener oscillations

The linear and nonlinear responses are obtained from the continuum effective α-$\mathcal{T}_3$ model that is valid for low-energy excitations. More experimentally relevant is the general lattice model. Here, using this model, we calculate the currents for the Kubo, Schwinger, and Bloch-Zener oscillation regimes. Figures 7(a) and 7(b) show that the ultrashort time transient, linear and nonlinear responses generated by the continuum effective model persist for the lattice model with the respective timescale increment factors h/W, $\sqrt{\hbar/(v_F e\mathcal{E})}$, $t_{\rm Bloch} \sim \hbar/(eaE)$, for any fixed electric field. In the Kubo regime, the total current $\widetilde{J}/\widetilde{E}$ still saturates. The consistency between Figs. 7(a), 7(b) and 4(a) suggests that the linear response can be used to detect the Berry phase. In the Schwinger regime, the current is the result of nonlinear response

$$\widetilde{J}/\widetilde{E} \propto \widetilde{E}^{1/2}\widetilde{t}, \tag{50}$$

as shown in Figs. 7(a) and 7(b).

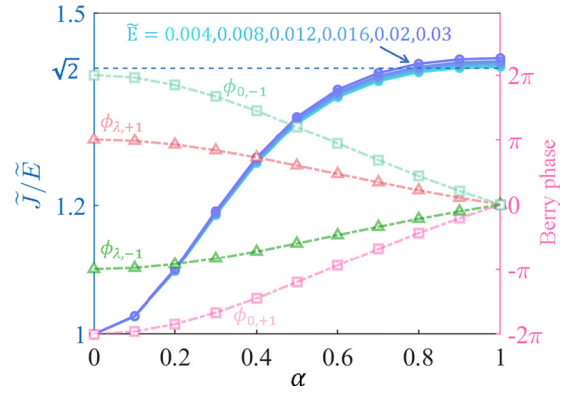

FIG. 8. Scaling law of the first peak of Bloch-Zener oscillations with the material parameter α. Shown are the scaling relations for different values of the electric field corresponding to the Berry-phase plots in Fig. 2 for quantum states from the conical and flat bands around the Dirac points $\pm K$.

In the Kubo regime where the timescale is larger than the classical time h/W, the interference between energy bands begins to contribute to the Landau-Zener transitions. In the Schwinger regime, the nonlinear response is dominated by the Landau-Zener transitions. For $Et_{\rm Bloch} \sim \hbar/(ea)$, Bloch oscillations occur. The combination of the Landau-Zener transition and Bloch oscillation leads to Bloch-Zener oscillations, as shown in Figs. 7(c) and 7(d) for $\alpha = 0,\ 1$, where the Bloch time period is $\widetilde{t}_B = 4\pi/(\sqrt{3}\widetilde{E})$. The decay of the amplitude and the irregular behavior of the Bloch-Zener oscillations in α-$\mathcal{T}_3$ lattice are the result of mixed interference of quantum states in multiple bands modulated by the geometric and dynamic phases [40]. For a range of the electric field, the timescales of the ultrashort transient and linear responses can be neglected compared with that of the nonlinear response. In this case, the first peak in the Bloch-Zener oscillations displays a scaling law, as shown in Fig. 8.

Taken together, the first peak in the Bloch-Zener oscillations, the nonlinear response, and the saturated current associated with the linear response all depend monotonically on the material parameter α. These physical quantities can then be exploited to detect the Berry phase.

IV. DISCUSSION

The Berry phase in the α-$\mathcal{T}_3$ lattice varies monotonically with the material parameter α. We investigated electronic transport when an α-$\mathcal{T}_3$ lattice system is driven by a constant electric field and calculated a number of current densities as a function of α in both the linear (Kubo) and nonlinear (Schwinger) response regimes. Remarkably, the current density also exhibits a monotonic dependence on α, implying that the Berry phase as a fundamental material characteristic can be determined by measuring the current (e.g., using graphene for calibration).

The various experimentally relevant scaling behaviors of the current density concerning the electric field and time as well as the underlying state transitions are summarized in Fig. 9. Depending on the product $\tilde{E}\tilde{t}$ of the normalized electric field and time, five distinct scaling regimes arise. For

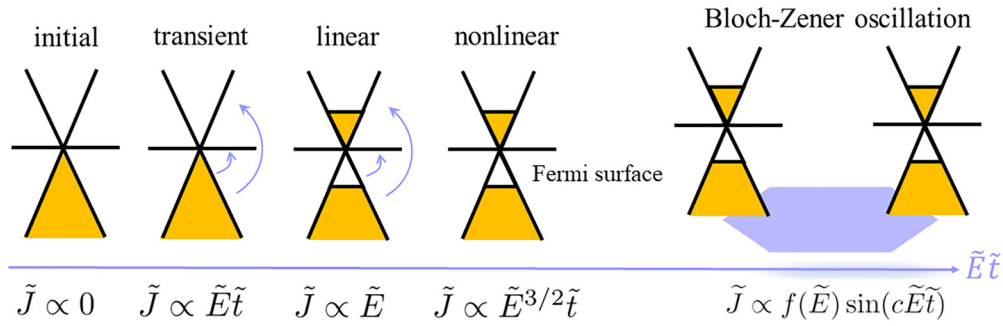

FIG. 9. Summary diagram: scaling behaviors, transitions, and physical mechanisms associated with ballistic transport in α-$\mathcal{T}_3$ lattice on different timescales.

$\tilde{E}\tilde{t} \sim 0$, the current density is zero. In the transient phase, the current density is proportional to $\tilde{E}\tilde{t}$. The linear response regime comes after the transient phase, in which the current is proportional just to the electric field. In the nonlinear response regime that follows the linear regime, the current is proportional to $\tilde{E}^{3/2}\tilde{t}$. For much larger values of $\tilde{E}\tilde{t}$, Bloch-Zener oscillations arise, whose amplitude can be an irregular function of time [40]. While the scenario in Fig. 9 is based on the effective continuum Hamiltonian, direct calculations of the lattice Hamiltonian indicate that the ultrashort time transient response, linear and nonlinear responses still arise. In fact, Landau-Zener transitions begin to occur in the linear response regime and become dominant in the nonlinear response regime. When $\tilde{E}\tilde{t}$ is comparable to a quantity of the same physical dimension determined by the lattice constant, Bloch-Zener oscillations occur. In this case, the first peak of the oscillation exhibits a scaling law with α by the nonlinear response mechanism when the ultrashort time transient and linear responses are negligible. Consequently, the linear and nonlinear responses can be exploited for experimental detection of the Berry phase, so can the Bloch-Zener oscillations, as the timescale around the time for the first oscillation peak to occur is currently experimentally feasible [51].

Zitterbewegung oscillations are not exclusive to Dirac electrons [52]. They have been experimentally observed in various physical systems characterized by a linear dispersion, such as ultracold atoms [53], photonic crystals [54], Bose-Einstein condensate [55,56], and photonic microcavities [57]. *Zitterbewegung* provides a physical interpretation for the minimal conductivity in graphene [48] and conductance fluctuations in quantum wells [58], and offers a calculation method for the optical conductivity [59,60]. These oscillations can be interpreted as a measurable consequence of the momentum-space Berry phase, as the amplitude of *Zitterbewegung* is modulated by the Berry phase [18,53,59,61]. A plausible mechanism for *Zitterbewegung* is the interference between the positive- and negative-energy solutions of the Dirac equation [18] in the effective low-energy approximation model. For the α-$\mathcal{T}_3$ lattice, the *Zitterbewegung* effect has been less studied [18]. In our work, we calculated the linear response in quantum transport, which reveals an interplay between *Zitterbewegung* and Berry phases in both the lattice and the low-energy effective models of α-$\mathcal{T}_3$.

In a previous work [62], a semiclassical treatment of Dirac electrons in the effective α-$\mathcal{T}_3$ model was developed. In particular, under a finite mass potential, the Wentzel-Kramers-Brillouin (WKB) semiclassical method was employed to investigate the transmission of the Dirac electrons, where the finite-mass potential opens up a gap in the energy spectrum. In our work, there is no energy gap due to the absence of a mass potential. We incorporated a time-dependent vector potential into the momentum to study the interaction of massless Dirac electrons with an electric field. At the present, developing a semiclassical theory to understand the electric currents in α-$\mathcal{T}_3$ lattice subject to an electric field is difficult because of the prerequisites for applying the WKB approximation. These include a potential that varies slowly compared to the wavelength of the particle, energy levels not being too close to the turning points, and consideration of the Klein tunneling effect of the relativistic quantum nature, etc.

ACKNOWLEDGMENTS

This work was supported by the Air Force Office of Scientific Research under Grant No. FA9550-21-1-0186.

[1] S. Pancharatnam, Generalized theory of interference, and its applications. Part I. Coherent pencils, Proc. Indian Acad. Sci. USA **44**, 247 (1956).

[2] H. C. L. Higgins, U. Öpik, M. H. L. Pryce, and R. A. Sack, Studies of the Jahn-Teller effect II the dynamical problem, Proc. R. Soc. London A **244**, 1 (1958).

[3] M. V. Berry, Quantal phase factors accompanying adiabatic changes, Proc. R. Soc. London A **392**, 45 (1984).

[4] D. Xiao, M.-C. Chang, and Q. Niu, Berry phase effects on electronic properties, Rev. Mod. Phys. **82**, 1959 (2010).

[5] Y. B. Zhang, Y. W. Tan, H. L. Stormer, and P. Kim, Experimental observation of the quantum Hall effect and Berry's phase in graphene, Nature (London) **438**, 201 (2005).

[6] P. Carmier and D. Ullmo, Berry phase in graphene: Semiclassical perspective, Phys. Rev. B **77**, 245413 (2008).

[7] K. S. Novoselov, E. McCann, S. V. Morozov, V. I. Fal'ko, M. I. Katsnelson, U. Zeitler, D. Jiang, F. Schedin, and A. K. Geim, Unconventional quantum Hall effect and Berry phase of 2π in bilayer graphene, Nat. Phys. **2**, 177 (2006).

[8] E. Illes, J. P. Carbotte, and E. J. Nicol, Hall quantization and optical conductivity evolution with variable berry phase in the α-$\mathcal{T}_3$ model, Phys. Rev. B **92**, 245410 (2015).

[9] C.-Z. Wang, C.-D. Han, H.-Y. Xu, and Y.-C. Lai, Chaos-based Berry phase detector, Phys. Rev. B **99**, 144302 (2019).

[10] A. K. Geim and K. S. Novoselov, The rise of graphene, Nat. Mater. **6**, 183 (2007).

[11] A. K. Geim and I. V. Grigorieva, Van der Waals heterostructures, Nature (London) **499**, 419 (2013).

[12] P. Ajayan, P. Kim, and K. Banerjee, Two-dimensional van der Waals materials, Phys. Today **69**(9), 38 (2016).

[13] L. Duca, T. Li, M. Reitter, I. Bloch, M. Schleier-Smith, and U. Schneider, An Aharonov-Bohm interferometer for determining Bloch band topology, Science **347**, 288 (2015).

[14] J. F. Rodriguez-Nieva and L. S. Levitov, Berry phase jumps and giant nonreciprocity in Dirac quantum dots, Phys. Rev. B **94**, 235406 (2016).

[15] F. Ghahari, D. Walkup, C. Gutiérrez, J. F. Rodriguez-Nieva, Y. Zhao, J. Wyrick, F. D. Natterer, W. G. Cullen, K. Watanabe, T. Taniguchi *et al.*, An on/off Berry phase switch in circular graphene resonators, Science **356**, 845 (2017).

[16] R. A. Sepkhanov, J. Nilsson, and C. W. J. Beenakker, Proposed method for detection of the pseudospin-$\frac{1}{2}$ Berry phase in a photonic crystal with a Dirac spectrum, Phys. Rev. B **78**, 045122 (2008).

[17] T. Biswas and T. K. Ghosh, Magnetotransport properties of the α-$\mathcal{T}_3$ model, J. Phys.: Condens. Matter **28**, 495302 (2016).

[18] T. Biswas and T. K. Ghosh, Dynamics of a quasiparticle in the α-$\mathcal{T}_3$ model: Role of pseudospin polarization and transverse magnetic field on Zitterbewegung, J. Phys.: Condens. Matter **30**, 075301 (2018).

[19] L. Tamang, T. Nag, and T. Biswas, Floquet engineering of low-energy dispersions and dynamical localization in a periodically kicked three-band system, Phys. Rev. B **104**, 174308 (2021).

[20] B. Dey and T. K. Ghosh, Photoinduced valley and electron-hole symmetry breaking in α-$\mathcal{T}_3$ lattice: The role of a variable Berry phase, Phys. Rev. B **98**, 075422 (2018).

[21] D. Oriekhov and S. Voronov, Size effects on atomic collapse in the dice lattice, J. Phys.: Condens. Matter **36**, 125603 (2024).

[22] L. Tamang and T. Biswas, Probing topological signatures in an optically driven α-$\mathcal{T}_3$ lattice, Phys. Rev. B **107**, 085408 (2023).

[23] A. Raoux, M. Morigi, J.-N. Fuchs, F. Piéchon, and G. Montambaux, From dia- to paramagnetic orbital susceptibility of massless fermions, Phys. Rev. Lett. **112**, 026402 (2014).

[24] C.-D. Han and Y.-C. Lai, Optical response of two-dimensional Dirac materials with a flat band, Phys. Rev. B **105**, 155405 (2022).

[25] Y.-R. Chen, Y. Xu, J. Wang, J.-F. Liu, and Z. Ma, Enhanced magneto-optical response due to the flat band in nanoribbons made from the α-$\mathcal{T}_3$ lattice, Phys. Rev. B **99**, 045420 (2019).

[26] L. Chen, J. Zuber, Z. Ma, and C. Zhang, Nonlinear optical response of the α-$\mathcal{T}_3$ model due to the nontrivial topology of the band dispersion, Phys. Rev. B **100**, 035440 (2019).

[27] J. J. Wang, S. Liu, J. Wang, and J.-F. Liu, Integer quantum Hall effect of the α-$\mathcal{T}_3$ model with a broken flat band, Phys. Rev. B **102**, 235414 (2020).

[28] J. D. Malcolm and E. J. Nicol, Magneto-optics of massless Kane fermions: Role of the flat band and unusual Berry phase, Phys. Rev. B **92**, 035118 (2015).

[29] F. Wang and Y. Ran, Nearly flat band with Chern number C= 2 on the dice lattice, Phys. Rev. B **84**, 241103(R) (2011).

[30] G. Giovannetti, M. Capone, J. van den Brink, and C. Ortix, Kekulé textures, pseudospin-one Dirac cones, and quadratic band crossings in a graphene-hexagonal indium chalcogenide bilayer, Phys. Rev. B **91**, 121417(R) (2015).

[31] B. Dóra and R. Moessner, Nonlinear electric transport in graphene: quantum quench dynamics and the Schwinger mechanism, Phys. Rev. B **81**, 165431 (2010).

[32] J. Schwinger, On gauge invariance and vacuum polarization, Phys. Rev. **82**, 664 (1951).

[33] L. Landau, On the theory of transfer of energy at collisions II, Phys. Z. Sowjetunion **2**, 118 (1932).

[34] C. Zener, Non-adiabatic crossing of energy levels, Proc. R. Soc. London A **137**, 696 (1932).

[35] F. Bloch, Quantum mechanics of electrons in crystal lattices, Z. Phys. **52**, 555 (1929).

[36] C. Zener, A theory of the electrical breakdown of solid dielectrics, Proc. R. Soc. London A **145**, 523 (1934).

[37] F. Dreisow, A. Szameit, M. Heinrich, T. Pertsch, S. Nolte, A. Tünnermann, and S. Longhi, Bloch-Zener oscillations in binary superlattices, Phys. Rev. Lett. **102**, 076802 (2009).

[38] L.-K. Lim, J.-N. Fuchs, and G. Montambaux, Bloch-Zener oscillations across a merging transition of dirac points, Phys. Rev. Lett. **108**, 175303 (2012).

[39] S. xia, Y. Zhang, Z. Li, L. Qin, C. Yang, H. Lu, J. Zhang, X. Zhao, Z. Zhu *et al.*, Band evolution and Landau-Zener Bloch oscillations in strained photonic rhombic lattices, Opt. Express **29**, 37503 (2021).

[40] L.-L. Ye and Y.-C. Lai, Irregular Bloch-Zener oscillations in two-dimensional flat-band Dirac materials, Phys. Rev. B **107**, 165422 (2023).

[41] V. Ivakhnenko, S. N. Shevchenko, and F. Nori, Nonadiabatic Landau–Zener–Stückelberg–Majorana transitions, dynamics, and interference, Phys. Rep. **995**, 1 (2023).

[42] P. O. Kofman, O. V. Ivakhnenko, S. N. Shevchenko, and F. Nori, Majorana's approach to nonadiabatic transitions validates the adiabatic-impulse approximation, Sci. Rep. **13**, 5053 (2023).

[43] J. Wang, J. F. Liu, and C. S. Ting, Recovered minimal conductivity in the α-$\mathcal{T}_3$ model, Phys. Rev. B **101**, 205420 (2020).

[44] H.-C. Kao, M. Lewkowicz, and B. Rosenstein, Ballistic transport, chiral anomaly, and emergence of the neutral electron-hole plasma in graphene, Phys. Rev. B **82**, 035406 (2010).

[45] S. A. Sato and A. Rubio, Nonlinear electric conductivity and THz-induced charge transport in graphene, New J. Phys. **23**, 063047 (2021).

[46] S. Vajna, B. Dóra, and R. Moessner, Nonequilibrium transport and statistics of Schwinger pair production in Weyl semimetals, Phys. Rev. B **92**, 085122 (2015).

[47] Z. Okvátovity, L. Oroszlány, and B. Dóra, Time-dependent electric transport in nodal loop semimetals, Phys. Rev. B **104**, 035130 (2021).

[48] M. Katsnelson, Zitterbewegung, chirality, and minimal conductivity in graphene, Eur. Phys. J. B **51**, 157 (2006).

[49] N. V. Vitanov and B. M. Garraway, Landau-Zener model: Effects of finite coupling duration, Phys. Rev. A **53**, 4288 (1996).

[50] C.-Z. Wang, H.-Y. Xu, L. Huang, and Y.-C. Lai, Nonequilibrium transport in the pseudospin-1 Dirac-Weyl system, Phys. Rev. B **96**, 115440 (2017).

[51] B. Rosenstein, M. Lewkowicz, H.-C. Kao, and Y. Korniyenko, Ballistic transport in graphene beyond linear response, Phys. Rev. B **81**, 041416(R) (2010).

[52] T. M. Rusin and W. Zawadzki, Zitterbewegung of electrons in graphene in a magnetic field, Phys. Rev. B **78**, 125419 (2008).

[53] J. Y. Vaishnav and C. W. Clark, Observing zitterbewegung with ultracold atoms, Phys. Rev. Lett. **100**, 153002 (2008).

[54] X. Zhang, Observing Zitterbewegung for photons near the Dirac point of a two-dimensional photonic crystal, Phys. Rev. Lett. **100**, 113903 (2008).

[55] C. Qu, C. Hamner, M. Gong, C. Zhang, and P. Engels, Observation of Zitterbewegung in a spin-orbit-coupled Bose-Einstein condensate, Phys. Rev. A **88**, 021604(R) (2013).

[56] L. J. LeBlanc, M. Beeler, K. Jimenez-Garcia, A. R. Perry, S. Sugawa, R. Williams, and I. B. Spielman, Direct observation of Zitterbewegung in a Bose-Einstein condensate, New J. Phys. **15**, 073011 (2013).

[57] S. Lovett, P. M. Walker, A. Osipov, A. Yulin, P. U. Naik, C. E. Whittaker, I. A. Shelykh, M. S. Skolnick, and D. N. Krizhanovskii, Observation of Zitterbewegung in photonic microcavities, Light Sci. Appl. **12**, 126 (2023).

[58] Y. Iwasaki, Y. Hashimoto, T. Nakamura, and S. Katsumoto, Conductance fluctuations in InAs quantum wells possibly driven by Zitterbewegung, Sci. Rep. **7**, 7909 (2017).

[59] D. O. Oriekhov and V. P. Gusynin, Optical conductivity of semi-Dirac and pseudospin-1 models: Zitterbewegung approach, Phys. Rev. B **106**, 115143 (2022).

[60] D. O. Oriekhov, V. P. Gusynin, and V. M. Loktev, Orbital susceptibility of T-graphene: Interplay of high-order van Hove singularities and Dirac cones, Phys. Rev. B **103**, 195104 (2021).

[61] J. Cserti and G. Dávid, Relation between Zitterbewegung and the charge conductivity, Berry curvature, and the Chern number of multiband systems, Phys. Rev. B **82**, 201405(R) (2010).

[62] N. Weekes, A. Iurov, L. Zhemchuzhna, G. Gumbs, and D. Huang, Generalized WKB theory for electron tunneling in gapped α-$\mathcal{T}_3$ lattices, Phys. Rev. B **103**, 165429 (2021).